A method of three dimensional thermo-fluid simulation of the receiver of a standard parabolic trough collector

M. Islam[1,2], Suvash C. Saha[1*], and M. A. Karim[1]

[1]*Faculty of Science and Engineering, School of Chemistry, Physics and Mechanical Engineering, Queensland University of Technology, Brisbane, QLD 4001, Australia*
[2]*Department of Mechanical Engineering, Chittagong University of Engineering and Technology, Chittagong-4349, Bangladesh.*
**Corresponding author: s_c_saha@yahoo.com*

Abstract

A Parabolic Trough Collector (PTC) is the most proven collector system for indirect steam generation in solar thermal power plants. However, the solar Irradiance Profile (IP) around the radiated surface of the receiver of this collector is likely to be highly non-uniform. Moreover, the outer surface of a bare receiver is disposed to convection and radiation heat loss. A three-dimensional (3D) Computational Conjugate Heat Transfer (CCHT) model of a bare receiver of Luz Solar 2 (LS2) PTC was developed. The CCHT model was developed applying Finite Volume (FV) technique of the state-of-the-art Computational Fluid Dynamics (CFD). The IP around the receiver surface of the collector was calculated applying the Monte Carlo Ray Tracing (MCRT) technique. The MCRT calculated IP was considered as heat flux boundary condition around the computational domain of the receiver applying special MCRT-FV coupling technique. Moreover, the heat loss from the receiver surface was calculated solving one-dimensional energy balance equation at the face of boundary cells. The CCHT model and the MCRT model were developed using ANSYS FLUENT and ZEMAX software products respectively. The MCRT-FV coupling and the heat loss calculation were facilitated using a User-Defined-Function (UDF).The CCHT model was verified with experimental results, and reasonably a good agreement between the measured value and the simulated results was obtained. The method of this CCHT modelling and its verification are described in this chapter. Moreover, the MCRT calculated IP functions specific to the LS2 collector are given for facilitating further CCHT modelling of the collector system.

Key words: LS2 collector; parabolic trough collector; PTC; computational fluid dynamics; CFD; conjugate heat transfer modeling.

1.1 INTRODUCTION

Parabolic Trough Collector (PTC) is a mature and widely used concentrating collector technology in the solar energy field (Grena 2009, Yang *et al.* 2010). A PTC, as shown in Figure 1, consists of a single axis North-South tracking (parallel to YZ plane) Parabolic Trough (PT) concentrating mirror that focuses solar radiation on to a receiver. The receiver, which, ideally, placed axially along the focal line (along X axis) of the mirror, consists of a Receiver Tube (RT) and an evacuated Glass Tube (GT) envelop. The receiver is the main part of the trough collector system that used to convert solar radiation to thermal energy.

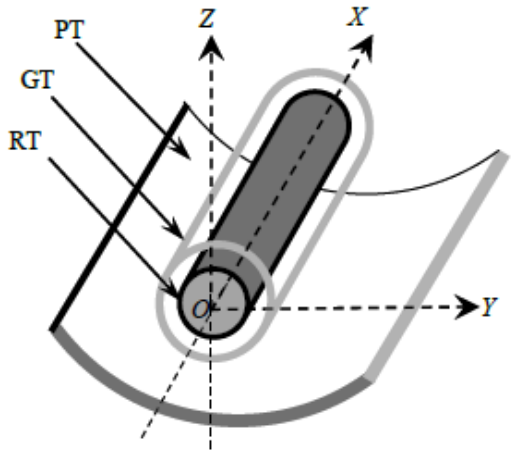

Figure 1: Basics of the PTC: (a) Cross-sectional view with nomenclature and (b) 3D view of a typical PTC. (In the figure, PT, GT and RT termed as parabolic trough, glass tube and receiver tube respectively)

The spectral energy harnessing process of the collector involves: incidence of solar radiation on mirror aperture, reflection and concentration of the incident energy onto to the outer surface of the receiver tube, and absorption of the radiant energy as thermal energy. Most of the radiant energy is conducted to the inner surface of the receiver tube as thermal energy due to temperature gradient developed by inducing forced convection heat transfer [1] phenomenon. Some suitable Heat Transfer Fluid (HTF) is used to induce the phenomenon. This is an example of a coupled heat transfer problem with complex geometry condition; this, and fairly similar concepts have been studied theoretically as well as experimentally by many researchers.

A buoyancy-driven flow and heat transfer in a narrow annular gap between co-axial, horizontal cylinders have been investigated experimentally and computationally by Vafai et al. (1997), Hamad and Khan (1998) and Dyko et al. (1999) on different occasions. Using an elliptic-cylinder coordinate system, Borjini et al. (1999) computationally studied combined radiation and free convection in a participating medium between two horizontal con-focal elliptical cylinders. The laminar natural convection in a differentially heated horizontal bare and finned rhombic annulus filled with air has been studied computationally by Farinas et al. (1999). Investigations specific to the trough solar collector have also been conducted remarkably in recent years.

Dudley *et al.* (1994) have investigated energy performance of Luz Solar 2 parabolic trough collector applying an extensive experimental procedure. R. Forristall (2003) has developed a detailed 1D and 2D heat transfer models of a parabolic trough solar collector's linear receiver to implement in Engineering Equation Solver (EES) for determining its performance. Kassem (2007) computationally investigated the free convection heat transfer in the annular space between the receiver tube and the glass envelope. He has considered an isothermal condition for the glass envelop, and a sinusoidal local heat flux distribution for the receiver tube. Reddy and his research team (2008a, 2008b, 2009) computationally have found a better performance for the collector using a porous receivers. Neglecting nonlinearity effect on heat loss, and assuming constant solar radiation, S.D. Odeh et al. have established a detailed thermal model to calculate the heat loss of trough collector [10]. Later the model has been used by Hou Z. et al. to analyse thermal efficiency of a trough system [11]. Effects of the realistic non-uniform heat flux distribution boundary condition on the conjugate heat transfer phenomenon of the collector system has been studied theoretically by different researchers. Ya-Ling He et al. has simulated the heat transfer process inside the absorber tube, and analysed the characteristics under the influence of the non-uniform heat flux distribution. They have established a coupled numerical method of Monte Carlo Ray Tracing (MCRT) and Finite Volume Method (FVM) to obtain the 3D flow fields and temperature distribution for the coupled heat transfer problem in absorber tube. Tao and He (2010) have developed a unified computational model for the coupled heat transfer process inside the receiver tube and the annuli space between the receiver tube and the glass envelop of the collector.

The foregoing literature review confirms that a lot of investigations have been performed to reveal energy performance and conjugate heat transfer phenomenon of the receiver with evacuated glass envelop, and heat transfer phenomenon inside the annuli space between the receiver and the glass envelop. However, infect the annuli space is not always evacuated, and many a times the glass envelop is either broken or removed. Therefore, the receiver is exposed to its surroundings, and experiences both free convection and radiation heat loss. This article details a method of computational modeling of a bare receiver of a standard parabolic trough collector.

The receiver tube of the Luz Solar 2 (LS2) PTC from Dudley *et al.*(1994) was modelled and simulated. The irradiance distribution around the receiver tube, which was calculated using the MCRT technique, was integrated with the FV model applying a special MCRT-FV coupling technique. Usually there is no evacuated glass cover around the CPV/T receiver. Therefore, several test conditions of the bare receiver of the LS2 collector were simulated. As the receiver was bare to the environment, special care was taken in calculating the radiation heat loss and the convection heat loss from the receiver walls. Moreover, the flow condition at the inlet was considered as being fully developed flow. A comprehensive approach was adopted to verify the accuracy of the FV model. Typical results of the simulation were also presented. A finite volume based software package, ANSYS Fluent 15.0, was used for this computational conjugate heat transfer modelling and simulation.

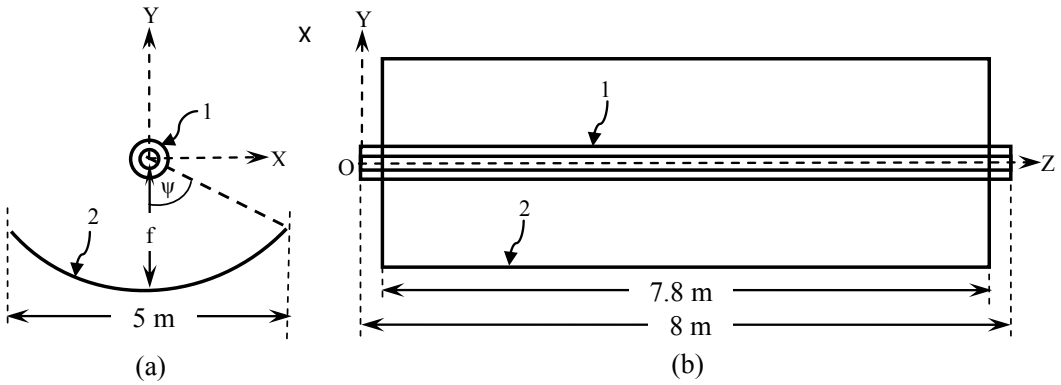

Figure 2: Schematic of the LS2 collector on the OXYZ coordinate system: (a) cross-section on XY plane, and (b) longitudinal view from the top on XZ plane. (In the figure:1 and 2 refer the evacuated receiver and the parabolic mirror respectively, f is the focal length (=1.84m), and ψ is the rim angle of the mirror (≈70°)).

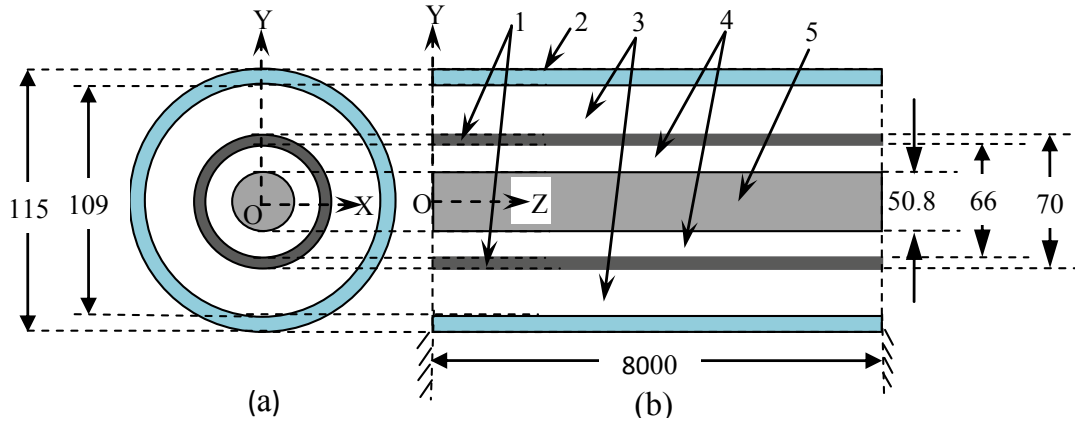

Figure 3: The geometry of the LS2 collector receiver on the OXYZ coordinate system: (a) angular cross-section on XY plane, and (b) longitudinal cross-section on YZ plane. (In the figure, 1, 2, 3, 4 and 5 refer to the absorber tube, glass tube, evacuated passage between the glass tube and the absorber tube, heat transfer fluid passage and the flow restriction device respectively. The dimensions are in mm).

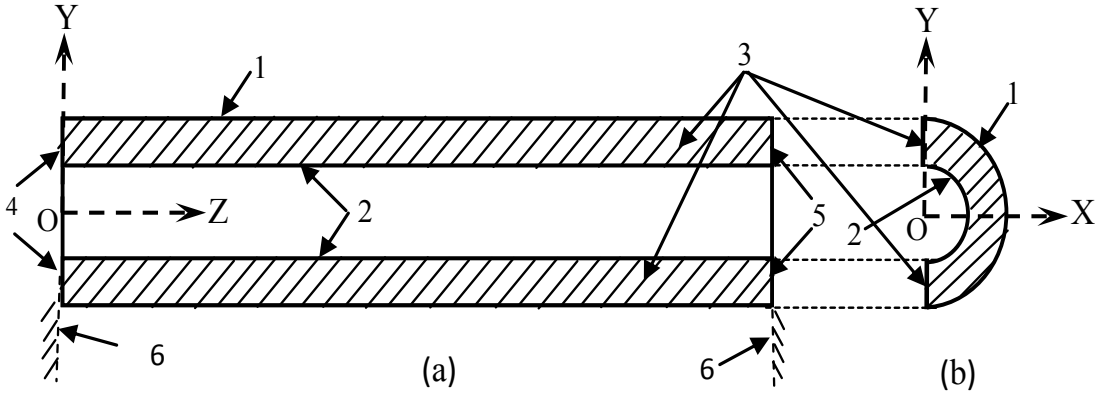

Figure 4: Heat Transfer Fluid (HTF) domain for the Finite Volume (FV) model on the OXYZ coordinate system, and the boundary conditions: (a) the longitudinal cross-section of the domain on YZ plane, and (b) the angular cross-section on XY plane. (In the figure, the numerals 2, 3, 4, 5 and 6 refer to non-slip heat flux wall, non-slip adiabatic inside wall, symmetry, fully developed velocity inlet, fully developed pressure outlet, and adiabatic ends of the receiver respectively).

1.2 PHYSICAL MODEL

The LS2 PTC was used in the Solar Energy Generating System (SEGS) III-VII 150 MW plants, Kramer Junction, California, USA; which is a proven solar collector for solar thermal electricity generation (Dudley, Kolb et al. 1994). The geometric configuration of the collector and the receiver are shown in Figure 2 and Figure 3 respectively. The mirror aperture is 5×7.8 m^2, and the receiver tube is 8 m long with 66 mm inner diameter and 2 mm wall thickness. In order to increase the flow velocity of the Heat Transfer Fluid (HTF), Dudley *et al.* (1994) inserted a 50.8 mm diameter closed-end plug inside the receiver tube. The HTF was Syltherm800 silicone based oil. The LS2 collector module was tested on the AZTRAK rotating platform at Sandia National Laboratory (SNL) by Dudley *et al.*(1994). Thermal energy performances of the collector under three physical conditions relating to the glass envelope of the receiver: (i) the glass envelope was evacuated, (ii) lost vacuum or air inside the envelope and (iii) removed glass cover or bare receiver was investigated. As has been mentioned earlier, since, the glass cover has direct contact with the photovoltaic (PV) solar cells of a CPV/T collector; the convection loss, along with the radiation loss, must take place from the PV surface to the environment. Therefore, to account for this environmental effect on the CPV/T collector receiver, the bare receiver of the LS2 collector was modelled for the current finite volume (FV) simulation so that the heat losses could be simulated and verified.

The irradiance distribution along the periphery of the receiver tube of the LS2 collector under ideal conditions, applying the MCRT optical simulation technique, as explained in Chapter 3, was found perfectly symmetric to the plane of geometric symmetry of the collector (Y-Z plane in Figure 2). Therefore, the HTF domain of right hand side half of YZ plane was modelled as shown in Figure 4 so as to minimize the computational expense utilizing of the characteristics of physical symmetry. The flow restriction device and the metal tube were not modelled for this conjugate heat transfer analysis as the flow properties were assumed steady state. Therefore, the shape of the computational domain was semi-cylindrical and horizontal. Gravity was acting vertically downward along the Y-axis. Several test conditions with the bare receiver of the collector as presented in Table 1 were selected for the current simulation.

Table 1: Selected test conditions of the bare receiver of the LS2 collector from Dudley *et al.*(1994).

Test conditions	DNI (W/m^2)	T_{amb} (°C)	T_{in} (°C)	V_{HTF} (m/s)	Re	T_{out} (°C)	V_{air} (m/s)
1st	919	22.6	301.4	0.608157	12710.1	318	0.1
2nd	867.6	19.8	203.4	0.597403	6431.098	219.6	0.5
3rd	929.8	21.8	252.2	0.606962	9218.136	269	1
4th	941.1	13.5	313.1	0.667897	14950.33	322	8
5th	961.3	15.1	313.3	0.667897	14967.46	320.7	9.3

DNI = Daily Normal Insolation, T = Temperature, V = Velocity, Re = Reynolds number, HTF = Heat Transfer Fluid, amb = ambient, in = inlet, and out = outlet.

1.3 COMPUTATIONAL MODEL DEVELOPMENT

1.3.1 Governing equations

As the minimum Reynolds number (Re) was more than 6000, the flow criteria of the selected test conditions as shown in Table 1 were turbulent considering the critical Reynolds number, Re_c 4000; incompressible; and steady state (Dudley, Kolb et al. 1994). The turbulent energy production, κ and the turbulent energy dissipation, ε were calculated using the RNG κ-εtransport equations. The governing equations and the transport equations were as given below:

The mass conservation equation or the continuity equation can be expressed in differential form as:

The mass continuity equation could be simplified as a volume continuity equation for Sylltherm800 oil at steady state condition as:

$$\nabla \bullet u_i = \frac{\partial u}{\partial x} + \frac{\partial v}{\partial y} + \frac{\partial w}{\partial z} = 0 \quad (1)$$

Considering the gravity along the global -*y* direction, the momentum equations for a three-dimensional (3D) steady state incompressible flow can be rewritten as

$$\rho(u\frac{\partial u}{\partial x}+v\frac{\partial u}{\partial y}+w\frac{\partial u}{\partial z})=-\frac{\partial p}{\partial x}+(\mu+\mu_t)\left\{\frac{\partial^2 u}{\partial x^2}+\frac{\partial^2 u}{\partial y^2}+\frac{\partial^2 u}{\partial z^2}\right\} \quad (2)$$

$$\rho(u\frac{\partial v}{\partial x}+v\frac{\partial v}{\partial y}+w\frac{\partial v}{\partial z})=-\frac{\partial p}{\partial y}+(\mu+\mu_t)\left\{\frac{\partial^2 v}{\partial x^2}+\frac{\partial^2 v}{\partial y^2}+\frac{\partial^2 v}{\partial z^2}\right\}-\rho g_y \quad (3)$$

$$\rho(u\frac{\partial w}{\partial x}+v\frac{\partial w}{\partial y}+w\frac{\partial w}{\partial z})=-\frac{\partial p}{\partial z}+(\mu+\mu_t)\left\{\frac{\partial^2 w}{\partial x^2}+\frac{\partial^2 w}{\partial y^2}+\frac{\partial^2 w}{\partial z^2}\right\} \quad (4)$$

where, μ and μ_t were the molecular viscosity and turbulent (eddy) viscosity respectively.

The conservation of energy equation was based on the energy balance that can be computed by the formula

$$\rho c_p\frac{\partial T}{\partial t}+\rho c_p\nabla.(u_i T)=-\nabla p+\left[k+\frac{c_p\mu_t}{\mathrm{Pr}_t}\right]\nabla^2 T+(\mu+\mu_t)\frac{\partial u_i}{\partial x_j}\left\{\frac{\partial u_i}{\partial x_j}+\frac{\partial u_j}{\partial x_i}-\frac{2}{3}\frac{\partial u_k}{\partial x_k}\delta_{ij}\right\}+S_r \quad (5)$$

where, S_r is solar radiation source term.

Two transport equations for RNG κ-ε model to calculate the turbulent energy production, κ and the turbulent energy dissipation, ε were

$$\frac{\partial}{\partial t}(\rho\kappa)+\nabla.(\rho\kappa u_i)=\alpha_\kappa(\mu+\mu_t)\nabla^2\kappa+G_\kappa+G_b-\rho\varepsilon \quad (6)$$

and

$$\frac{\partial}{\partial t}(\rho\varepsilon)+\nabla.(\rho\varepsilon u_i)=\alpha_\varepsilon(\mu+\mu_t)\nabla^2\varepsilon+C_{1\varepsilon}\frac{\varepsilon}{\kappa}(G_\kappa+C_{3\varepsilon}G_b)-\rho C_{2\varepsilon}^*\frac{\varepsilon^2}{\kappa} \quad (7)$$

respectively.

where, $C_{1\varepsilon}$ and $C_{3\varepsilon}$were two model constants equal to 1.42 and 1.68 respectively, G_κ and G_b were turbulent kinetic energy generation due to mean velocity gradient and buoyancy effect respectively, and α_κ and α_ε were the inverse effective Prandtl numbers for κ and ε and respectively.

Eddy viscosity was modified for swirl generation in the RNG model as

$$\mu_t = \rho C_\mu \frac{\kappa}{\varepsilon} f(\alpha_s, \Omega, \frac{\kappa}{\varepsilon}) - \rho C_{2\varepsilon}^* \frac{\varepsilon^2}{\kappa} \quad (8)$$

where, $C_\mu = 0.0845$, α_s was the swirl constant roughly set to *0.07* for mild swirl flows and even higher value can be set for a strong swirl flow, and Ω was a characteristics swirl number that was calculated inside the ANSYS Fluent.

Table 2: Temperature (K) dependent correlations for the HTF physical properties.

Properties	$=a + bT + cT^2 + dT^3 + eT^4$ +----------					Temperature range (K)
	a	*b*	*c*	*d*	*e*	
ρ(kg/m³)	1139.2	-0.546	-4.87e-04			233 to 673
c_p(J/kg K)	1108.2	1.7073				233 to 673
k (W/m K)	0.1901	-1.88e-04				233 to 673
μ (Pa s)	0.2591	-8.93e-04				233 to 273
	0.157	-8.00e-04	1.03e-06			273 to 340
	0.0848	-5.54e-04	1.39e-06	-1.57e-09	6.67e-13	340 to 673
$k_{Steel} = 15.906 + 0.0025T^2 + 5e\text{-}05T^3$ W/mK						
ρ = Density, c_p = isobaric heat capacitance, k = thermal conductivity, μ = dynamic viscosity.						

1.3.2 Physical properties of the computational domain

The constituent of the computational domain as shown in Figure 4 was the Syltherm800 fluid. The physical properties including the density, isobaric heat capacitance, thermal conductivity and the dynamic viscosity of the HTF were correlated with its instantaneous absolute temperature. The polynomial correlations were developed as given in Table 2. The tube material, which was not modelled, was steel, and the thermal conductivity of steel, k_{Steel} was also correlated with its absolute temperature as included in the same table.

1.3.3 Assumptions and the boundary conditions of the computational domain

As Figure 4 shows, the boundary conditions in the computational domain were: 1: no-slip heat flux wall, 2: no-slip adiabatic wall, 3: symmetry, 4: fully developed velocity inlet and pressure outlet, and 5: adiabatic ends of the receiver. They are explained in details below.

The no-slip heat flux wall: The inside surface and the outside surface of the absorber tube formed this non-slip heat flux boundary wall of the computational domain. The outside surface of the tube was exposed directly to the concentrated solar radiation and the environment; and the inside one was in direct contact with the viscous, pressurized and incompressible HTF. Shell conduction in the wall was active.

The outside surface of the tube was absorbing the incident solar irradiation energy as heat flux, and the inside surface was losing the heat energy to the flowing HTF. Simultaneously, because of the environmental effect, the outside surface was also losing some of the heat energy due to the radiation and convection heat losses. The rate of the concentrated solar energy and its density distribution around the receiver tube was calculated by applying the MCRT technique, which was coupled with the current FV model applying a special coupling technique as discussed in Section 1.3.4. The theoretical framework and the calculation technique of the heat loss from the outside surface of the tube are described in Section 1.3.5.

On the other hand, the convective and the conductive energy transfer from the inside surface of the tube to the HTF were calculated applying the built-in finite volume technique of the ANSYS Fluent software package. Moreover, the inside surface of the tube was assumed sufficiently frictional to form a non-slip wall to the viscous HTF.

The no-slip adiabatic wall*:* The circumferential surface of the cylindrical flow restriction device that was immersed into the viscous, pressurized and incompressible HTF as shown in Figure 3 formed this wall boundary condition. The surface of the devise was assumed sufficiently frictional to the HTF to form a non-slip boundary. On the other hand, at steady state condition, no energy exchange between the device and the HTF was assumed.

As the RNG κ-ε turbulence model was not that efficient in calculation of the flow parameters near the wall, standard wall functions developed by Launder and Spalding (1974) were used for near wall treatment. The logarithmic law-of-the-wall for mean velocity is given by the following formula:

$$U^* = \frac{\ln(Ey^*)}{\kappa} \tag{9}$$

where, $U^* \equiv \left(U_P C_\mu^{0.25} K_P^{0.25}\right)/\left(\tau_w/\rho\right)$, $y^* \equiv \left(\rho C_\mu^{0.25} K_P^{0.25} y_P\right)/\mu$, κ = von Kármán constant (= 0.4187), E = empirical constant (= 9.793), U_P = mean velocity of the fluid at point P, K_P = turbulence kinetic energy at point P, y_P = distance from point P to the wall, and μ = dynamic viscosity of the fluid.

This law is only valid for y^* between 30 and 300. In Fluent, the log-law is employed when y^* of the mesh adjacent to the wall is larger than 11.225. But the laminar stress-strain relationship, $U^* = y^*$ is used for the values smaller than 11.225. The laws-of-the-wall for mean velocity and temperature are based on the wall unit, y^*, rather than y^+ ($\equiv \rho u_\tau y/\mu$). However, these quantities are approximately equal in equilibrium turbulent boundary layers.

Symmetry: The shape of the HTF domain in between the absorber tube and the flow restriction device was annular or hollow cylindrical. The thickness of the annulus was assumed to be perfectly uniform. Moreover, the incident concentrated light around the external surface of the annulus was found symmetric either side of the YZ plane (see Figure 3) along the periphery. The HTF flow inside the annulus was assumed symmetric with respect to the YZ plane. Therefore, the flow criteria and the conjugate heat transfer characteristics were assumed symmetric to the YZ plane.

Fully developed velocity inlet and pressure outlet: As the HTF inlet of the computational domain of the modelled receiver was downstream of a sufficiently long close-channel flow line, the flow of Syltherm800 viscous oil inside the no-slip annulus at the inlet must be fully developed turbulent flow. The flow was simulated as fully developed flow instead of assuming simplistic average fluid velocity such that (Cheng, He et al. 2012):

$$\frac{\partial u_i}{\partial z} = \frac{\partial k}{\partial z} = \frac{\partial \varepsilon}{\partial z} = \frac{\partial p}{\partial z} = \frac{\partial T}{\partial z} = 0 \tag{10}$$

Adiabatic edges: The rest of the HTF flow line except the computational domain enclosed within the HTF inlet and outlet was assumed perfectly insulated, therefore, no or negligible heat losses were assumed from inlet and outlet edges of the domain. Moreover, the bracket loss at the steady state condition was also assumed negligible.

1.3.4 Coupling between MCRT and FV models

As explained in Section 1.3.3, the non-slip heat flux boundary wall was absorbing the concentrated light that was reflected from the parabolic trough mirror. The distribution of the irradiance along the periphery of the computational domains of the both the receiver elements were calculated using a well verified MCRT model. The irradiance distribution around the receiver was calculated as the Local Concentration Ratio (LCR). The integration between the MCRT and the FV models in the literature could be found sharing the same local irradiance data table by the models (Cheng, He et al. 2010; He, Xiao et al. 2011; Cheng, He et al. 2012) provided that the grid at the outer surfaces of the physical model was the same, and the analysis of the optical and thermal behaviour of the collector were simultaneous and dependent. On the contrary, a unique approach for the current FV model was adopted in which both models shared the same irradiance profile yet they were completely independent in their grid system and analysis.

Predicting the LCR profiles of the LS2 receiver for a large number of test conditions, two sets of polynomial correlations were developed applying the curve fitting technique as a function of angular location, β (°) of the receiver. Using the correlations, the local irradiance around the receiver with evacuated glass envelope and without glass envelope could be calculated. The correlations with their coefficients of determination, R^2 were given by the following set of equations for the receiver with glass envelope:

$$
\begin{aligned}
&I_{0^\circ\le\beta\le15^\circ} = C_1\times(2.8e-3\times\beta^3 - 1.29e-2\times\beta^2 + 0.1333\times\beta + 43.333),\\
&(R^2 = 0.9973)\\
&I_{15^\circ<\beta\le48^\circ} = C_1\times(6.98e-3\times\beta^2 - 0.108\times\beta + 52.414),(R^2 = 0.9988)\\
&I_{48^\circ<\beta\le90^\circ} = C_1\times(1.2849e-3\times\beta^3 - 0.2622\times\beta^2 + 15.74\times\beta - 229.49),\\
&(R^2 = 0.9999)\\
&I_{90^\circ<\beta\le180^\circ} = C_1\times(-1.06e-4\times\beta^2 + 4.24e-2\times\beta - 2.9507),(R^2 = 0.9973)
\end{aligned}
\qquad (11)
$$

and without glass envelope:

$$I_{0^\circ\le\beta\le15^\circ} = C_2\times(1.98e-4\times\beta^4 - 3e-3\times\beta^3 + 2.37e-2\times\beta^2 + 3.59e-2\times\beta + 46.453),(R^2 = 0.9857)$$

$$I_{15^\circ<\beta\le48^\circ} = C_2\times(1.19e-4\times\beta^3 - 4.1e-3\times\beta^2 + 0.2074\times\beta + 49.602),(R^2 = 0.997) \quad (12)$$

$$I_{48^\circ<\beta\le90^\circ} = C_2\times(1.230434e-3\times\beta^3 - 0.2511\times\beta^2 + 15.012\times\beta - 214.19),(R^2 = 0.9999)$$

$$I_{90^\circ<\beta\le180^\circ} = C_2\times(-1.055e-4\times\beta^2 + 4.19e-2\times\beta - 2.9121),(R^2 = 0.9954)$$

where, C_1 = DNI×ρ_{PT}×τ_{GT}×α_{RT}, C_2 = DNI×ρ_{PT}×α_{RT}, R^2 = Coefficient of determination and DNI = Daily Normal Insolation (W/m^2).

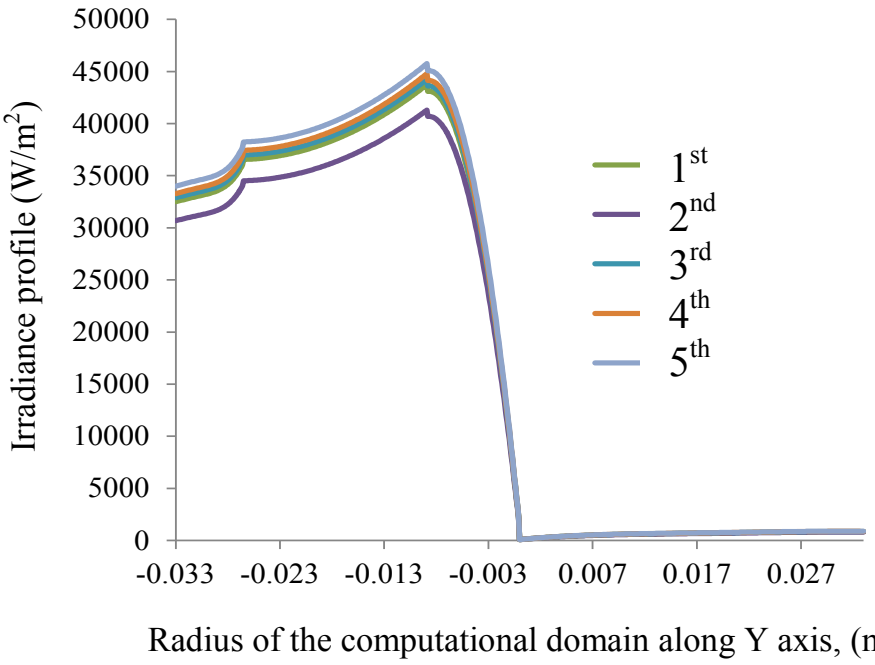

Figure 5 Calculation of the irradiance distribution along the circumference of the computational domain using the set of correlations of Equation (12)

The irradiance distributions along the circumference of the computational domain for the selected test conditions as presented in Table 1 were calculated using the set of correlations (12) as shown in Figure 5. As the DNI for the most of the test conditions were very close, the irradiance profiles were also found very close to each other.

Incorporating the correlations, an in-house subroutine was developed by using the ANSYS macros, which was interpreted in the FV model. The solar energy in the macro was treated as heat flux and surface phenomenon of the domain. The irradiance profile was assumed uniform along the tube length. At the inlet and outlet, each edges of the receiver tube was larger than the mirror by 100 mm, therefore, was shaded (see Figure 2). The macro enabled a grid independent coupling between the MCRT and the FV model. The heat loss from the outside wall of the domain to the environment by means of radiation and convection was also incorporated in the same macro applying the following theories.

1.3.5 The radiation and convection heat losses from the outside surface

As the absorber tube was bare, both the radiation and convection heat losses from the wall to the ambient were considered as surface phenomena. The following algorithm for the heat loss calculation was incorporated into the same MCRT-FV coupling macro.

The radiation heat loss was calculated by the formula

$$q_{rad} = \varepsilon\sigma[F_{gr}(T_w^4 - T_{gr}^4) + F_{sky}(T_w^4 - T_{sky}^4)] \tag{13}$$

where, ε was the emissivity of the cermet coated absorber tube that was given by, $\varepsilon = 0.000327T_w - 0.065971$ (Forristall 2003), σ was the Stefan-Boltzmann constant (=5.670373×10^{-8} W/m^2K^4), F was the radiation view factor, and T was temperature in Kelvin. The subscripts ‘gr’, ‘w’ and ‘sky’ referred to the ground, wall and the sky respectively.

The view factor between the receiver and the ground, F_{gr}, and between the receiver and the sky, F_{sky} were calculated respectively as:

$$F_{gr} = 0.5(1 + \cos\beta) \tag{14}$$

$$F_{sky} = 0.5(1 - \cos\beta)$$

where, β was the angular location on the receiver in OXY plane such that β = 0° along -OY axis and 180° along +OY axis (see Figure 4).

The ground temperature, $T_{gr} = T_a$, whereas, the sky temperature, $T_{sky} = T_a - 8$ (Forristall 2003). Here, the subscript 'a' refers to the air or ambient.

On the other hand, as the selected test conditions in Table 1 shows wind speed during the data collection, forced convection heat loss from the receiver surface was assumed. The loss per unit surface area was given by:

$$q_{convec} = h(T_w - T_a) \tag{15}$$

where, h was the force convection co-efficient. As the exact event was not known, h was calculated as average of leeward co-efficient, h_{lee} and wind-ward coefficient, h_{wind}. According to Sharples and Charlesworth (1998), these coefficients were calculated by,

$$h_{lee} = 2.2V_a + 8.3$$
$$h_{wind} = 3.3V_a + 6.5 \tag{16}$$

where, V was the velocity of air.

1.3.6 Grid generation technique for the computational domain of LS2 receiver

The accuracy and the stability of numerical simulation strongly rely on the grid resolution and distribution inside the computational domain. The mesh resolution should be fine enough, and the distribution should be reasonable to some regions of the domain in order to capture the flow physics properly; otherwise, an exaggerated result would be produced from the simulation. As the current computational simulation involves turbulent flow along the Z axis, and high temperature heat transfer across the XY plane from the wall to the viscous HTF, the grid resolution near the wall must be fine enough in order to capture the flow physics, that is, the viscous and thermal boundary layers near the frictional wall; and the grid must be distributed such a way that the effect of viscosity and heat transfer by means of convection (diffusion and advection) across the flow is resolved. Therefore, a structured and hexahedral grid system was

generated for the current computational domain in such a way that the grids were uniformly distributed along the HTF flow (see the grid system on the YZ plane at the Outside wall, and along the Z axis at the symmetry in Figure 6) and inflated by 10% across the flow from the wall to the centre of the bulk flow (see the grid system on the XY plane at the Inlet/Outlet face, and along the Y axis at the Symmetry in Figure 6). However, the optimum grid resolution was decided by performing the grid independence test as explained in Section 1.4.1.

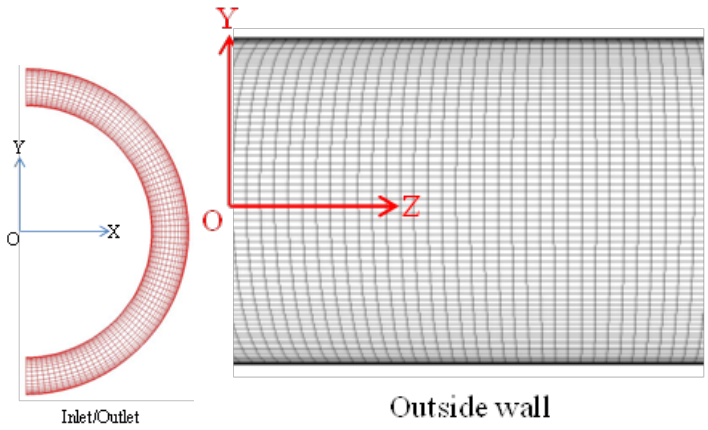

Figure 6 Grid structure distribution for the computational domain.

1.3.7 Solution method

The governing equations describing the current conjugate heat transfer fluid flow model were highly non-linear and coupled in nature that made them almost impossible to obtain an analytical solution applying by available knowledge. Instead an approximate numerical solution would be an efficient technique for this kind of real world problem. However, the accuracy and/or the acceptability of the solution to the experts simply relies on the adopted numerical scheme and the solution method.

The FV method was adopted for the current simulation to discretise the governing equations. The discretization was facilitated by employing one of the highly reliable FV based CFD software packages, ANSYS Fluent 14.5.

As the shell conduction within the material of the receiver was accounted for in the simulation, a segregated numerical method was selected between the segregated and coupled

(implicit and explicit)—two available solution methods in ANSYS Fluent. Using this approach, the governing equations were solved sequentially, that is, segregated from one another. As the governing equations are non-linear and coupled, several iterations of the solution loop must be performed before a converged solution is obtained. Any iteration consists of the steps as outlined below:

1. Fluid properties are updated, based on the initialized solution at the first iteration, and based on the current solution at the subsequent iteration.
2. In order to update the velocity field, the u, v, and w momentum equations are each solved in turn using current values for pressure and face mass fluxes,.
3. Since the velocities obtained in Step 2 may not satisfy the continuity equation locally, a "Poisson-type" equation for the pressure correction is derived from the continuity equation and the linearized momentum equations. This pressure correction equation is then solved to obtain the necessary corrections to the pressure and velocity fields and the face mass fluxes such that continuity is satisfied.
4. Where appropriate, equations for scalars such as turbulence, energy, and species are solved using the previously updated values of the other variables.
5. When interphase coupling is to be included, the source terms in the appropriate continuous phase equations may be updated with a discrete phase trajectory calculation.
6. A check for convergence of the equation set is made.
7. These steps are continued until the convergence criteria are met.

As the grid system of the current computational domain was hexahedron, and the upstream and the downstream of the domain were fully specified; in order to achieve a better accuracy in the simulation, a higher order Quadratic upwind differencing scheme: the QUICK scheme (Leonard and Mokhtari 1990) was adopted to discretise 3D convection-diffusion problem. Quick type schemes are based on a weighted average of second-order-upwind and central interpolations of the variable. However, undertaking calculations with a higher order differencing scheme like QUICK sometimes would experience an instability problem in the solution because of some reason like poor initial guess. In order to minimize this chance of instability, after the initialization of the solution, the calculation was accomplished in three different steps: (1) first 50 to 500 iterations with first order upwind scheme, (2) next 50 to 500

more iterations with the second order upwind scheme, and (3) finally resume the calculation until convergence of the solution activating the QUICK scheme. Because of the inherent limitations of the standard, linear, second order and body-force-weighted pressure interpolating schemes, the PRESTO! scheme was adopted for the current simulation as this particular scheme is applicable with all types of grid systems. In FLUENT, SIMPLE is the default pressure-velocity coupling technique. Therefore, the SIMPLE algorithm was selected for the current steady state and turbulent HTF flow model. In the present study, the under-relaxation factors were set as 0.3 for the pressure and momentum, 0.8 for turbulent dissipation rate, and 0.75 for the rest of the parameters.The maximum allowable residuals were set at 10^{-6} for the energy equation, and 10^{-4} for the rest of the parameters. However, at the end of the computations of the present FV model, the residuals of the most of the values were found to be a couple of order less than the set values.

1.4 VERIFICATION OF THE MODEL

1.4.1 Grid independence test to decide the optimum grid resolution

In Section 1.3.6, a grid generation technique for the computational domain of the LS2 receiver element was illustrated. In this section, how the optimum grid system for the receiver element was adopted is explained.

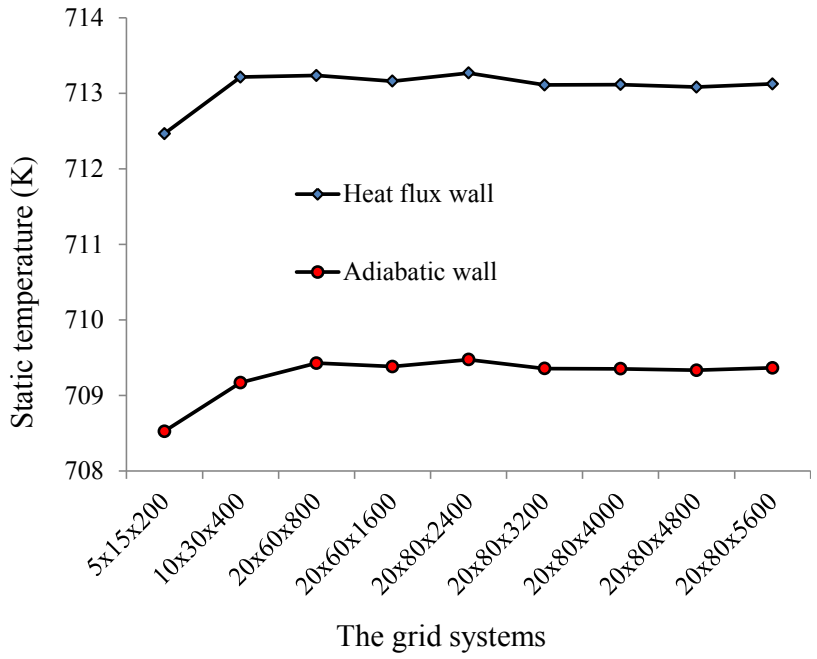

Figure 7 Grid independence test.

The grid independence test is an approximate measure of whether the grid system in a computational domain is optimally fine; otherwise the simulation result might be misleading. As the present FV model was a conjugate heat transfer simulation of steady state turbulent flow, the HTF temperature near the outlet of the domain was presumed to be the highest within the domain. Therefore, the optimum grid resolution was decided based on the effect of grid resolution on the static temperatures at two different locations on the heat flux wall (see Section 1.3.3) and the adiabatic wall (see Section 1.3.3) close to the HTF outlet. Nine different grid systems were generated, and the static temperature near the HTF outlet at two points on the inside and outside walls of the domain were calculated as shown in Figure 7. As the figure shows, analysing the variations in the recorded temperatures, the grid system $20_r \times 60_\beta \times 1600_z$ was found satisfactory for the current computational domain. Here, suffix r, β and z refer to the radial, angular/circumferential and longitudinal / Z axis direction of the domain. However, for further accuracy and to get maximum benefit of high performance computing (HPC) facilities at the Queensland University of Technology (QUT) the grid system $20_r \times 80_\beta \times 3200_z$ was chosen for the current model that produced 5120000 hexahedral cells.

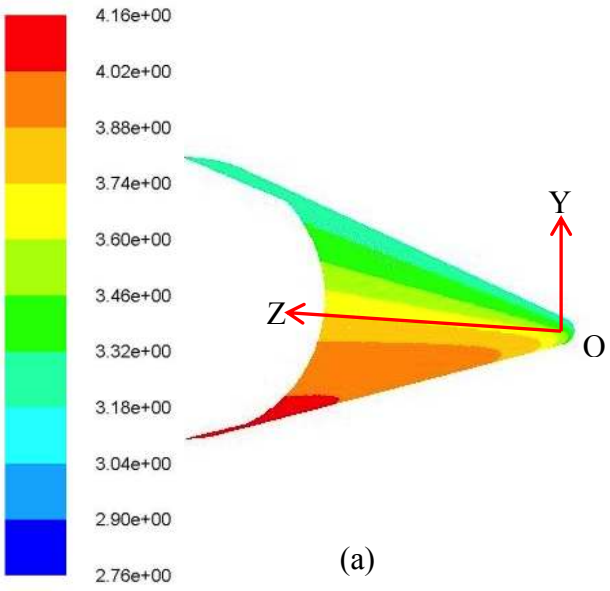

(a)

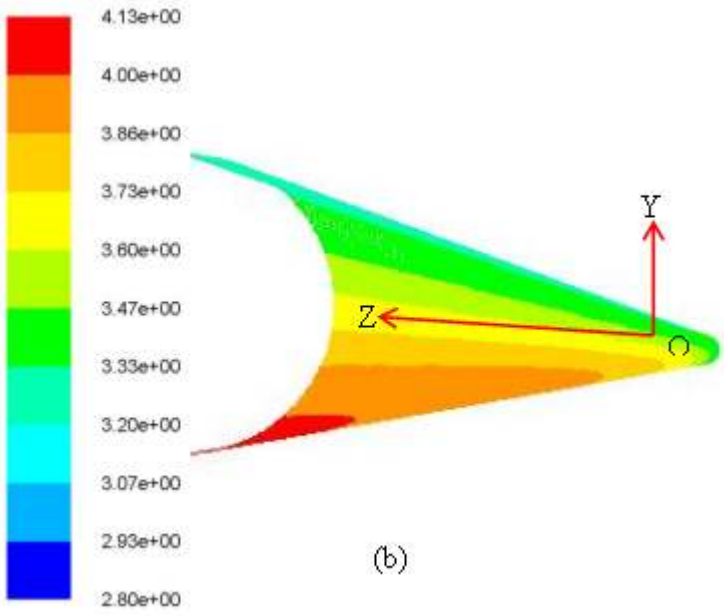

Figure8. Wall Y^* values: (a) at outside wall, and (b) at inside wall.

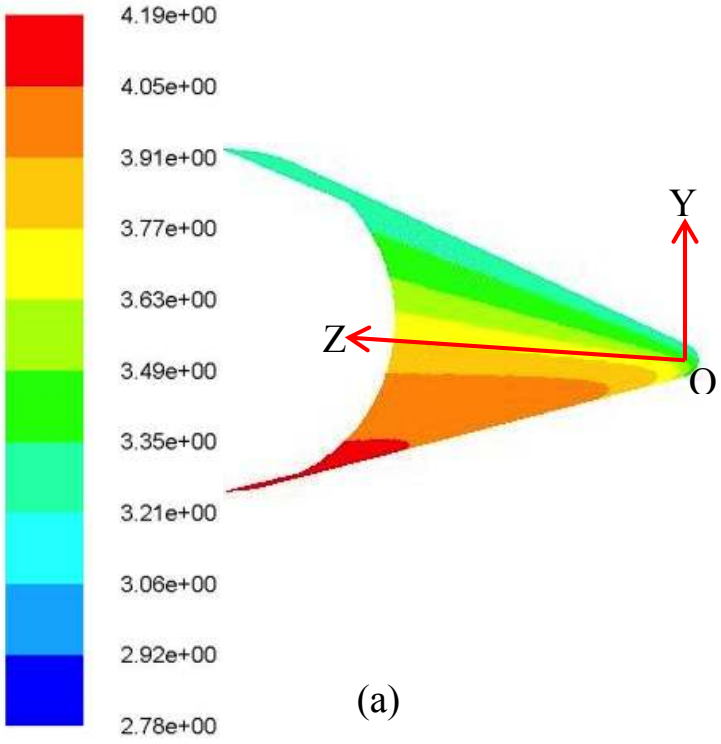

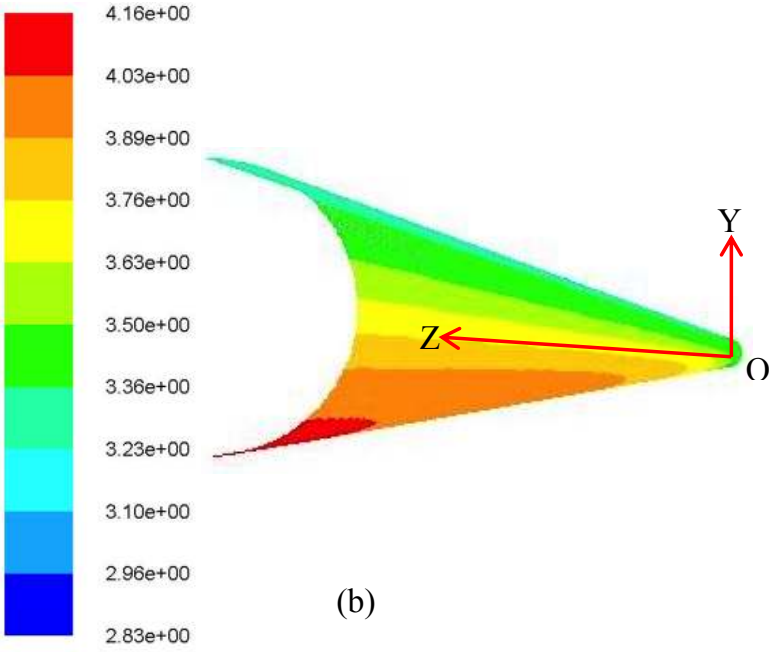

Figure 9: Wall Y^+ values: (a) at outside wall, and (b) at inside wall.

1.4.2 Checking the near wall grid resolution

The value of wall Y* and/or Y+ is an indication of whether the grid resolutions near the wall are fine enough, or the first cell adjacent to the wall is within the boundary layer so that the flow physics inside the computational domain near the no-slip wall is resolved properly. Lower values of Y* and the Y+ correspond to a fine mesh near the wall. Therefore, Y* and Y+ of both of the walls (the heat flux wall and the adiabatic wall) of the computational domain were calculated from the FV model as shown in Figure8 and 11 respectively. The figures show that the maximum Y* value was 4.16, and the maximum Y+ value was 4.19 on the outside wall near the HTF outlet where the temperature was maximum. As the maximum Y* value was lower than 11.225, the laminar stress-strain relationship was employed in calculation of this value (see the Section 1.3.3). The minimum values of Y* and Y+ were calculated 2.76 and 2.78 respectively, which were also could be found on the outside wall near the inlet edge where the temperature was minimum relative to the entire domain. That implies that the near wall grid resolution was fine enough.

Table 3: Comparison of model calculated results with experimental data.

TCs	DNI (W/m^2)	V_a (m/s)	T_a (°C)	T_{in} (°C)	T_{o_expt} (°C)	T_{o_model} (°C)	E_{abs} (%)	E_{av} (%)
1st	919	0.1	22.6	301.4	318	320.98	0.94	
2nd	867.6	0.5	19.8	203.4	219.6	213.19	2.92	
3rd	929.8	1	21.8	252.2	269	271.68	1.04	1.11
4th	941.1	8	13.5	313.1	322	322.73	0.23	
5th	961.3	9.3	15.1	313.3	320.7	322.08	0.43	

Acronyms: TC = Test Conditions, DNI = Daily Normal Insolation, V = Velocity, T = Temperature, E = Error. Suffixes: a = air or ambient, in = inlet, o_expt = experimental outlet data, o_model = model calculated outlet data, abs = absolute, av = average

1.4.3 Verification of the FV model and the MCRT-FV integration

The current FV model was used to calculate the HTF outlet temperature for five different test conditions for the bare receiver of LS2 collector. The outlet temperatures HTF of the simulated test conditions were compared with the experimental results as presented in Table 3. The maximum absolute error between the simulated results and the experimental results were calculated to be 2.92% for the second test condition, and the minimum absolute error was calculated to be 0.23% for the fourth test condition. The average absolute error was calculated to be 1.11%. This good agreement between the simulated results and the experimental results was validated the accuracy of the current FV model and the MCRT-FV integration macro.

Table 4: Comparison of outlet temperature at different heat loss conditions.

Test conditions	V_a	T_i	No loss model	Total loss model		Convection loss model		Radiation loss model	
			T_{o_Max}	T_{o_Min}	q_{loss_Max}	T_{o_Convec}	q_{loss_Convec}	T_{o_Rad}	q_{loss_Rad}
	(m/s)	(°C)	(°C)	(°C)	(%)	(°C)	(%)	(°C)	(%)
1st	0.1	301.4	325.45	320.98	18.60	322.20	13.52	324.18	5.30

2nd	0.5	203.4	215.90	213.19	21.64	213.57	18.65	215.51	3.11
3rd	1	252.2	275.94	271.68	17.91	272.21	15.69	274.94	4.21
4th	8	313.1	335.74	322.73	57.47	323.85	52.54	334.43	5.80
5th	9.3	313.3	336.43	322.08	62.05	323.18	57.28	335.11	5.71

In the table, V is velocity, T is temperature and q is heat energy per second. Suffix a, i, o, Max, Min, Convec and Rad stand for air, inlet, outlet, maximum, minimum, convection and radiation respectively.

1.4.4 Verification of the heat loss calculation algorithm

As the receiver was bare, ambient conditions strongly affected the convection and radiation heat losses from the surface of the computational domain. The loss was calculated using an in-house subroutine coupled with the MCRT-FV integration macro. The test conditions were simulated assuming four different heat loss conditions including, (i) no loss model, (ii) total loss model, (iii) convection loss model, and (iv) radiation loss model. The estimated HTF outlet temperature and the percentage of heat loss data were arranged in Table 4. One might understand from the general knowledge of heat transfer that the HTF outlet temperature would be the maximum without heat loss, the minimum with total loss (both convection and radiation hat losses), and in between these maximum and minimum temperatures with the convection heat loss and the radiation heat loss. The calculated outlet temperatures of the HTF under all four heat loss conditions as presented in the table support the general knowledge completely. This particular investigation confirmed the reliability of the heat loss algorithm that used in the in-house macro with the MCRT-FV integration macro.

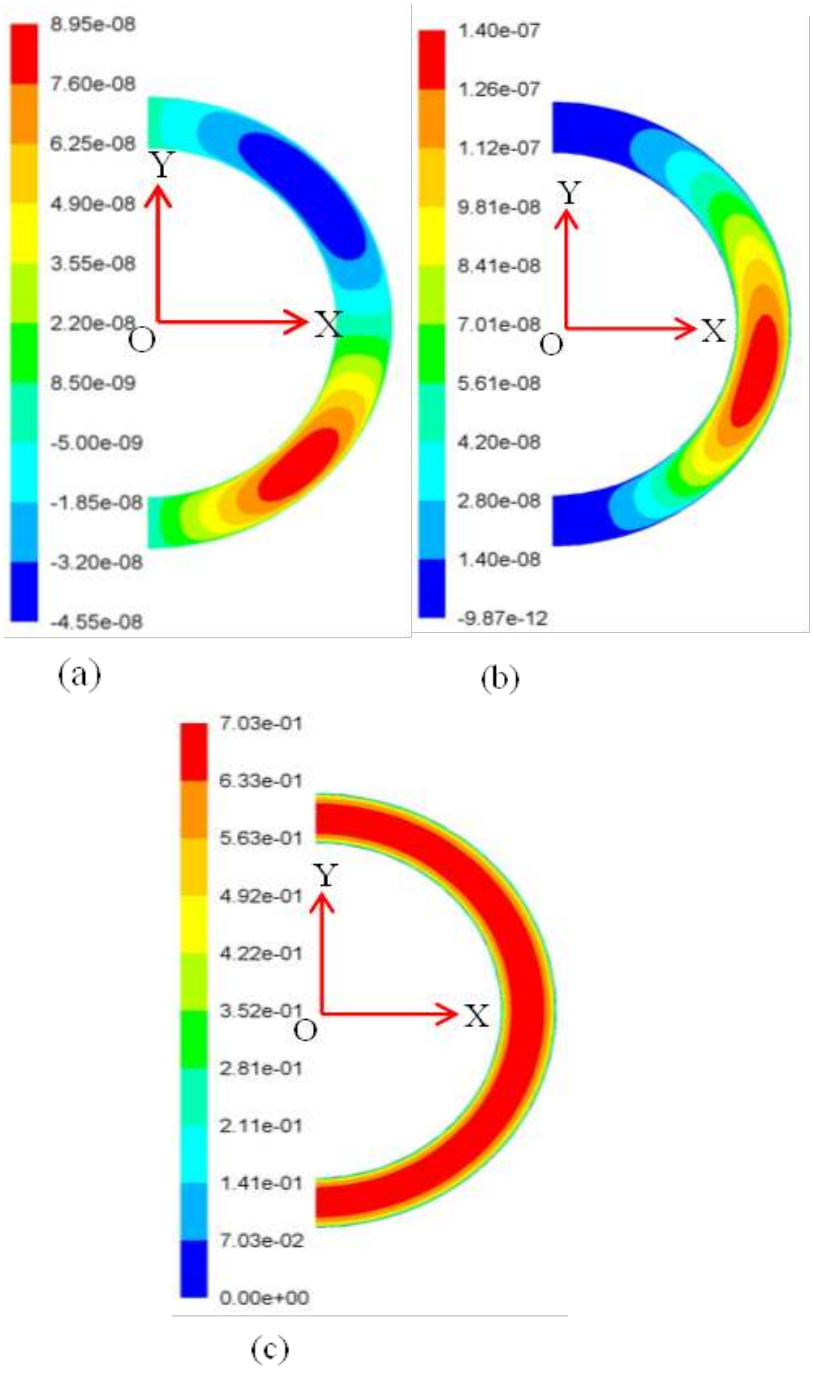

Figure 10: Velocity contour at the inlet: (a) X velocity, (b) Y velocity and (c) Z velocity.

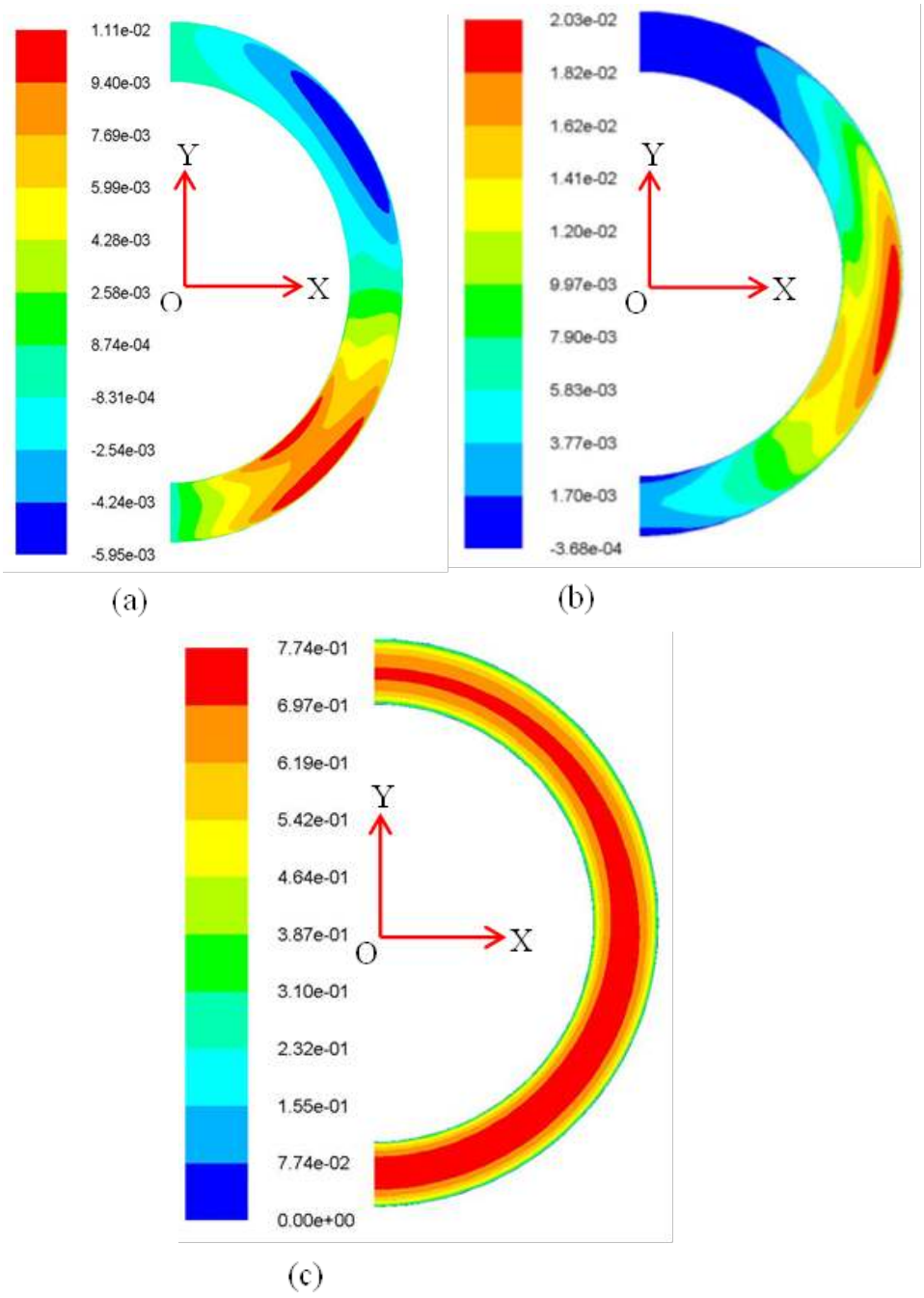

Figure 11: Velocity contour at the outlet: (a) X velocity, (b) Y velocity and (c) Z velocity

1.4.5 Checking the fully developed flow condition at the HTF inlet

As discussed in Section 1.3.3, the HTF flow at the inlet was considered fully developed instead of average bulk flow. Firstly, in case of the average velocity assumption, the longitudinal

velocity (the Z velocity for the current models) across the flow (from the wall to the bulk flow centre) is uniform and becoming fully developed along the downstream gradually or rapidly depending on the turbulence. Whereas, in case of the fully developed flow, the longitudinal velocity is zero adjacent to the wall due to a viscous share effect and developed fully at the bulk flow centre of the HTF where all of the flow properties are in steady state condition according to Equation (10). Secondly, the velocity components perpendicular to the bulk flow (the X and Y velocities for the current models) are zero in case of average or uniform velocity assumption, whereas, the components are non-zero at fully developed flow. Finally, the longitudinal or bulk flow velocity contours of a steady state flow at the inlet and outlet of a solved computational domain would be exactly similar to each other if the flow is isothermal and adiabatic; otherwise, would be fairly similar. The velocity contours at the HTF inlet, outlet and symmetry boundaries of the computational domains of both of the receiver elements were visually investigated and compared against these three criteria for the flow to be fully developed at the inlet.

The velocity contours at the HTF inlet and outlet boundaries of the computational domain of the LS2 receiver are shown in Figure 10 and Figure 11respectively. The longitudinal velocity profile and the Z velocity contour in Figure 10(c) match perfectly with the first criterion as the velocity near the wall is zero, and maximum at the centre. Moreover, the velocity components perpendicular to the axial velocity, the X velocity and the Y velocity in Figure 10(a) and (b) respectively, match perfectly with the second criteria as none of these components are non-zero. Finally, the axial velocity contour at the inlet (see Figure 10(c)) could be seen to match perfectly with that at the outlet (see Figure 11(c)). However, the dissimilarities, if any could be seen by visual investigation, between the velocity contours of X, Y and Z velocity components at the inlet (see Figure 10) and those components at the outlet (see Figure 11) were might be because of conjugate heat transfer effect across the flow. Nonetheless, it could be claimed that the simulation of the fully developed flow at the HTF inlet of the computational domain of the LS2 receiver was appropriate.

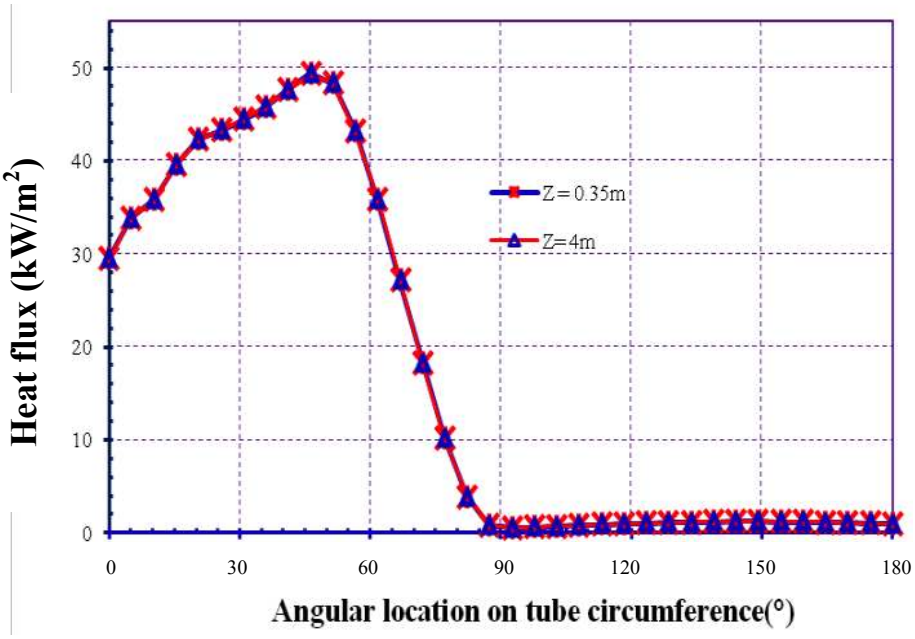

(a)

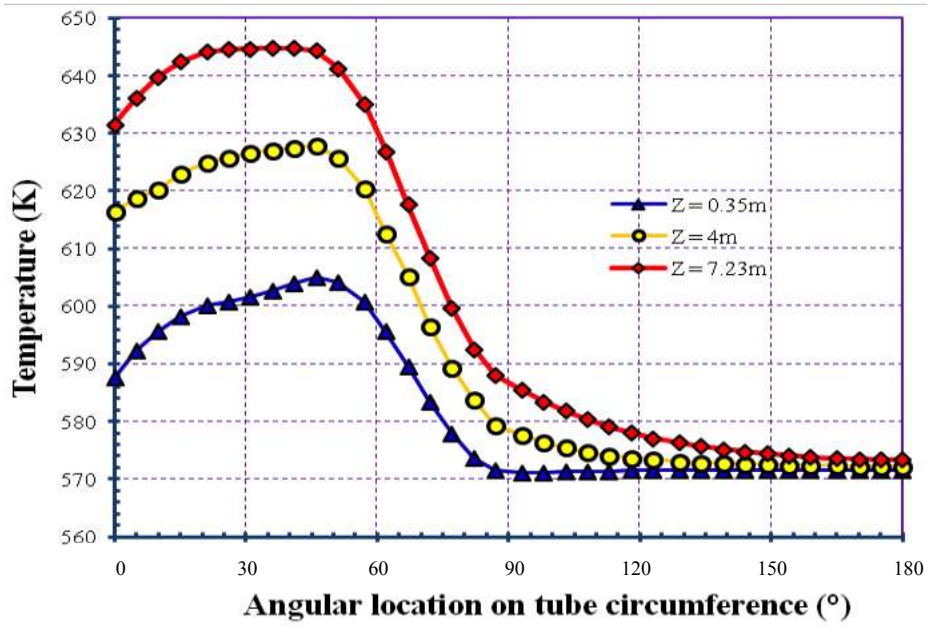

(b)

Figure 12: Thermal characteristics along the circumference of the computational domain: (a) resultant heat flux profile, and (b) the temperature profiles.

1.4.6 Further verification of the MCRT-FV integration

The accuracy of MCRT-FV integration was already justified in Section 1.4.3. However, the integration is further verified comparing the residual heat flux profile around the circumference of the computational domain as shown in Figure 14(a). The purpose of the integration was to reproduce a realistic and appropriate concentrated solar energy flux profile around the circumference of the computational domain as shown in Figure 5. Whether, the algorithm and the employed macro for the integration worked properly could be justified comparing the similarity between the input concentrated solar flux profile as shown in Figure 5 with the residual wall heat flux profile in Figure 14(a). However, the magnitude of the solar flux in Figure 5 could be seen much lower than the residual heat flux in Figure 14(a), which was because the residual heat flux was calculated for about 1000 W/m^2 DNI and at ideal conditions without considering any heat loss from the surface in contrast to the realistic test conditions as shown in Figure 5 for validation of the present FV model. Ignoring the discrepancy in the flux magnitude, the similarity of the both profiles confirmed the accuracy of the coupling and the in-house algorithm.

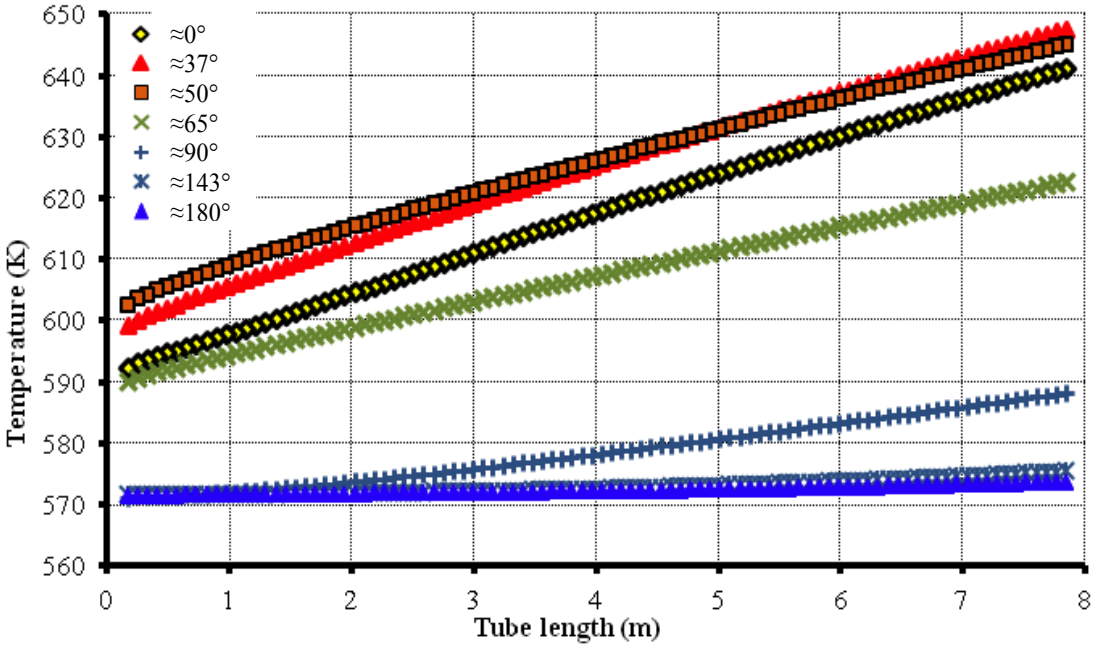

Figure 13: Longitudinal temperature profile along the length of the tube at different angular locations.

1.5 THERMAL CHARACTERISTICS OF THE LS2 RECEIVER

Using the present FV model, the heat loss from the receiver surface was investigated, and the resultant heat flux profile and the temperature profiles around the receiver surface were calculated as described below.

1.5.1 Heat loss phenomena

As the receiver was bare, and the operating temperature was significantly higher than that of the environment, the receiver must lose heat energy from its outer surface by virtue of temperature difference due to convection and radiation. The individual effect of both of these heat transfer modes were investigated as presented in Table 4.

In the table, the no loss model represents the maximum possible rise of HTF temperature without any heat loss. On the contrary side, the total loss model shows the minimum possible temperature rise of the HTF and maximum heat loss at the respective ambient conditions. On the other hand, the convection loss model and the radiation loss model show the effect of convection loss and the radiation loss on the HTF outlet temperature and the heat loss.

As the table shows, from the total loss model, the maximum heat loss increases moderately with the increase of ambient air velocity from 18% of heat energy with 0.1 m/s air velocity to as much as 62% of thermal energy with 9.3 m/s air velocity. The reason for this loss was the convection as could be seen from the convection loss model. Because, in the total loss, the radiation was found to account for around 5% of the heat energy loss, while the convection accounted for the rest of the thermal loss. It should be noted that the radiation loss directly depends on the temperature difference between the receiver and the environment, while the convection loss depends not only on the temperature difference but also on the air velocity of the environment. Therefore, maintaining an optimum evacuation level between the receiver tube and the glass envelop of a conventional PTC is important to check the convection loss. However, as a higher working temperature would decrease the electric performance of PV solar cells, heat loss from the PV aperture of a CPV/T collector might be beneficial for the cells' efficient operation.

1.5.2 Resultant heat flux and temperature profiles of the receiver outside wall

The current model was adapted to calculate the heat flux profile and the temperature profile around the receiver wall at ideal condition. The DNI for this particular investigation was considered about 1 sun. While the circumferential profiles are illustrated in Figure 12, the longitudinal profiles are presented in Figure 15.

As the Figure 12(a) shows, the heat flux profiles at 0.35 m length location and at 4 m length location of the receiver along the circumference were calculated that were found highly non-uniform and almost similar to that of the solar irradiance distribution. Since, both of the profiles were coincident, there was no or little variations in heat flux could be seen along the receiver length, which was reasonable as the incident solar flux along the length was assumed uniform.

Again Figure 12(b) shows the temperature profiles along the circumference of the receiver at 0.35 m, 4 m and 7.23 m length locations. The temperature profiles were found significantly non-uniform as was found for the heat flux profiles. Unlike the heat flux profile, the temperature was found to increase from the inlet to the outlet along the length of the tube, which was further supported from the longitudinal temperature profile of the receiver as shown in Figure 15. The increase in temperature, as the figure shows, from inlet to outlet edges of the receiver was found fairly linear.

For a standard PTC, the solar flux distribution along the receiver was found almost fixed. Therefore, it would be possible to decrease the temperature variations along the receiver circumference by increasing the HTF turbulence or HTF mixing inside the domain. The mixing of the HTF inside the receiver could be achieved by using some type of swirl generator such as twisted tape insert into the domain. The insert would induce a swirl or rotation effect into the fluid, so that the HTF may rotate at least 90° while flowing from the inlet to the outlet. By this way, the HTF inside the receiver tube would be heated more evenly, and the resultant temperature profile of the tube wall along the periphery might be gentler, which would not only increase the heat gain of the HTF but also would decrease the heat loss from the receiver surface.

1.6 CONCLUSION

A 3D FV model was developed. In order to be able to validate the FV model directly, the bare receiver of the LS2 collector was simulated, as the measured thermal efficiency data of the collector is available in the literature. The Reynolds ratio, Re_r (ratio of Reynolds number to a critical Reynolds number, 4000) of the selected test conditions were varied between 1.6 and 3.74. The heat flux wall was absorbing a non-uniformly distributed concentrated solar radiation, the distribution of which was calculated using the MCRT optical simulation model. The irradiance profile around the circumference of the computational domain was simulated applying MCRT technique and integrated with the FV model using an in-house macro. Radiation and convection loss from the outer surface of the receiver were incorporated in the macro.

The FV model was verified by comparing the calculated and measured HTF outlet temperature data. The absolute deviation between the numerical results and the measured data was estimated would to be maximum 2.92%, minimum 0.23% and average 1.11%. This very good agreement between the simulation results and the experimental data confirmed the reliability of the FV model, and the accuracy of the MCRT-FV integration.

The FV model was further used to investigate the combined and separate effects of convection heat loss and radiation heat loss. The combined heat loss was found increasing from 19% to 62% of maximum heat gain with the increase of air velocity from 0.1 m/s to 9.3 m/s. Among these losses, radiation loss was accountable for at most 6% of total loss, whereas the convection loss was accountable for the rest of the heat losses that refer to the importance of evacuated glass envelope around the receiver tube of a PTC. On the other hand, the resultant heat flux profiles and the temperature profiles along the periphery of the computational domain were found mostly similar to that of the incident irradiance distribution around the same receiver. While the resultant heat flux was found to be uniform along the length of the tube due to the uniform incident irradiance along the same direction, the temperature was found to gradually increase from the inlet to the outlet. The angular non-uniformity of the temperature profile of an ideal PTC demonstrates the importance of some swirl generator or twisted-tape inserts into the flow, which might increase the convection heat transfer into the heat transfer fluid by increasing the swirl or fluid mixing.

1.7 BIBLIOGRAPHY

ANSYS, I. (2011). "ANSYS FLUENT Theory Guide." from http://cdlab2.fluid.tuwien.ac.at/LEHRE/TURB/Fluent.Inc/v140/flu_th.pdf.

Cheng, Z. D., Y. L. He, et al. (2012). "Numerical simulation of a parabolic trough solar collector with nonuniform solar flux conditions by coupling FVM and MCRT method." Solar Energy **86**(6): 1770-1784.

Cheng, Z. D., Y. L. He, et al. (2010). "Three-dimensional numerical study of heat transfer characteristics in the receiver tube of parabolic trough solar collector." International Communications in Heat and Mass Transfer **37**(7): 782-787.

Dudley, V. E., G. J. Kolb, et al. (1994). Test results: SEGS LS-2 solar collector**:** p:139.

Forristall, R. (2003). Heat Transfer Analysis and Modeling of a Parabolic Trough Solar Receiver Implemented in Engineering Equation Solver, National Renewable Energy Laboratory, 1617 Cole Boulevard, Golden, Colorado 80401-3393, Technical report No. NERL/TP-550-34169.

He, Y.-L., J. Xiao, et al. (2011). "A MCRT and FVM coupled simulation method for energy conversion process in parabolic trough solar collector." Renewable Energy **36**(3): 976-985.

Launder, B. E. and D. B. Spalding (1974). "The numerical computation of turbulent flows." Computer Methods in Applied Mechanics and Engineering **3**(2): 269-289.

Leonard, B. P. and S. Mokhtari (1990). "Beyond first-order upwinding: The ultra-sharp alternative for non-oscillatory steady-state simulation of convection." International Journal for Numerical Methods in Engineering **30**(4): 729-766.

Sharples, S. and P. S. Charlesworth (1998). "Full-scale measurements of wind-induced convective heat transfer from a roof-mounted flat plate solar collector." Solar Energy **62**(2): 69-77.